Princeton Plasma Physics Laboratory

PPPL- 5213

A dynamic magnetic tension force as the cause of failed solar eruptions

Clayton E. Myers, Masaaki Yamada, Hantao Ji, Jongsoo Yoo, William Fox, Jonathan Jara-Almonte, Antonia Savcheva & Edward E. DeLuca

December 2015

Prepared for the U.S. Department of Energy under Contract DE-AC02-09CH11466.

Princeton Plasma Physics Laboratory
Report Disclaimers

Full Legal Disclaimer

This report was prepared as an account of work sponsored by an agency of the United States Government. Neither the United States Government nor any agency thereof, nor any of their employees, nor any of their contractors, subcontractors or their employees, makes any warranty, express or implied, or assumes any legal liability or responsibility for the accuracy, completeness, or any third party's use or the results of such use of any information, apparatus, product, or process disclosed, or represents that its use would not infringe privately owned rights. Reference herein to any specific commercial product, process, or service by trade name, trademark, manufacturer, or otherwise, does not necessarily constitute or imply its endorsement, recommendation, or favoring by the United States Government or any agency thereof or its contractors or subcontractors. The views and opinions of authors expressed herein do not necessarily state or reflect those of the United States Government or any agency thereof.

Trademark Disclaimer

Reference herein to any specific commercial product, process, or service by trade name, trademark, manufacturer, or otherwise, does not necessarily constitute or imply its endorsement, recommendation, or favoring by the United States Government or any agency thereof or its contractors or subcontractors.

PPPL Report Availability

Princeton Plasma Physics Laboratory:

http://www.pppl.gov/techreports.cfm

Office of Scientific and Technical Information (OSTI):

http://www.osti.gov/scitech/

Related Links:

U.S. Department of Energy

U.S. Department of Energy Office of Science

U.S. Department of Energy Office of Fusion Energy Sciences

A dynamic magnetic tension force as the cause of failed solar eruptions

Clayton E. Myers[1,2], Masaaki Yamada[2], Hantao Ji[1,2,3], Jongsoo Yoo[2], William Fox[2], Jonathan Jara-Almonte[1,2], Antonia Savcheva[4] & Edward E. DeLuca[4]

[1]*Department of Astrophysical Sciences, Princeton University, Princeton, New Jersey 08544, USA*

[2]*Princeton Plasma Physics Laboratory, Princeton, New Jersey 08543, USA*

[3]*Laboratory for Space Environment and Physical Sciences, Harbin Institute of Technology, Harbin, Heilongjiang 150001, China*

[4]*Harvard-Smithsonian Center for Astrophysics, Cambridge, Massachusetts 02138, USA*

Coronal mass ejections are solar eruptions driven by a sudden release of magnetic energy stored in the Sun's corona[1]. In many cases, this magnetic energy is stored in long-lived, arched structures called magnetic flux ropes[2–5]. When a flux rope destabilizes, it can either erupt and produce a coronal mass ejection or fail and collapse back towards the Sun[6–8]. The prevailing belief is that the outcome of a given event is determined by a magnetohydrodynamic force imbalance called the torus instability[9–14]. This belief is challenged, however, by observations indicating that torus-unstable flux ropes sometimes fail to erupt[15]. This contradiction has not yet been resolved because of a lack of coronal magnetic field measurements and the limitations of idealized numerical modelling. Here we report the results of a laboratory experiment[16] that reveal a previously unknown eruption criterion below which torus-unstable flux ropes fail to erupt. We find that such 'failed torus' events occur when the guide

magnetic field (that is, the ambient field that runs toroidally along the flux rope) is strong enough to prevent the flux rope from kinking. Under these conditions, the guide field interacts with electric currents in the flux rope to produce a dynamic toroidal field tension force that halts the eruption. This magnetic tension force is missing from existing eruption models, which is why such models cannot explain or predict failed torus events.

For a laboratory experiment to study ideal instability solar eruption mechanisms such as the torus instability, it must adhere to the standard storage-and-release model for solar eruptions. According to this model, eruptions are triggered by transient events in the corona rather than by dynamic changes at the solar surface[1]. For an arched flux rope, the relative invariance of the solar surface translates to a slow driving requirement at the two 'line-tied' (anchored) footpoints. Previous laboratory arched flux rope experiments[17–19] have deviated from the storage-and-release model by relying on the dynamic injection of either plasma or magnetic flux at the footpoints to produce an eruption. In contrast, the present experiments[16] enforce a strict separation of timescales between the footpoint driving time, τ_D, and the dynamic Alfvén time, τ_A, such that the observed eruptions must be driven by storage-and-release mechanisms (see Methods and Extended Data Tables 1 and 2).

Flux ropes in the solar corona are most susceptible to two ideal magnetohydrodynamic instabilities: the torus instability[9–14] and the kink instability[20–24] (see Methods). At present, the torus instability is thought to be the primary driver of eruptions[13], while the kink is believed to play a secondary part[7]. The onset criteria for these instabilities are inextricably linked to the ambient potential magnetic field (also known as the vacuum field) in which the flux rope is embedded. On the Sun, the potential field is produced by sources located beneath the solar surface, while in the laboratory it is produced by fixed magnetic field coils located outside the plasma (see Extended Data Fig. 1). In either case, the potential field can be decomposed into two orthogonal components: the strapping field, which runs perpendicular to the flux rope, and the guide field, which runs toroidally along it (see Extended Data Fig. 2). The strapping field is central to the torus instability in that it produces the strapping force, which counters the upward-driving 'hoop' force and restrains the flux rope (see Methods). The guide field, on the other hand, is central to the kink instability in that it reduces the magnetic twist in the flux rope (see Methods).

More quantitatively, the critical parameter for the torus instability is the potential field decay index[10], n, which characterizes the spatial decay of the potential field (a high n value indicates a steep spatial decay and hence torus instability; see Methods). Likewise, the critical parameter for the kink instability is the edge safety factor[25–27], q_a (where a is the edge minor radius of the flux rope), which characterizes the inverse magnetic twist in the flux rope (a low q_a value indicates a high twist and hence kink instability; see Methods). Our laboratory experiments facilitate the independent control of n and q_a, enabling us to systematically explore the torus versus kink instability parameter space and to identify the stability boundaries.

The n versus q_a parameter space is scanned in the experiment by independently modifying the magnitude and the vertical (z) profile of each potential field component. Figure 1 compares two representative flux rope plasmas with different potential field settings: the flux rope in Fig.

1c has high q_a and low n such that it is stable, while the flux rope in Fig. 1d has low q_a and high n such that it erupts violently and repeatedly towards the wall of the machine. These are just two examples from a comprehensive scan of n and q_a, the results of which are shown in Fig. 2. Four distinct parameter regimes are readily identified in the experimental data. Three of these (the stable, eruptive, and failed kink regimes) are consistent with the present understanding of the torus and kink instabilities. In particular, the kink instability appears below $q_a \simeq 0.8$ but does not necessarily drive an eruption. Only when the decay index also exceeds the observed torus threshold ($n \simeq 0.8$) does the failed kink regime give way to the eruptive regime (consistent with numerical simulations[7]). Interestingly, the observed torus threshold of $n \simeq 0.8$ is substantially lower than the theoretical expectation of $n = 3/2$. This reduced threshold is consistent with the theory of the 'partial torus instability', which accounts for the effect of the line-tied geometry on the hoop force[28]. The fourth instability regime identified in Fig. 2, which we call the 'failed torus' regime, contradicts the widely held notion that the torus criterion is a sufficient condition for eruption. In this regime, kink-stable flux ropes that exceed the torus threshold fail to erupt. This behaviour cannot be explained in terms of the hoop and strapping forces alone. Instead, a magnetic tension force related to the toroidal guide field plays a crucial part.

To examine more carefully the physics of the failed torus regime, magnetic field data from a characteristic failed torus event are shown in Fig. 3. The height-time evolution of this event (Fig. 3a) shows that the plasma initially rises before saturating and then rapidly collapsing downward. Clues as to why this occurs are found in spatial plots of the toroidal current density, J_T (Fig. 3d, see Extended Data Table 3 for descriptions of the various current and field components). The internal profile of J_T rapidly transforms from nearly uniform to strikingly hollow during the failed torus event. This hollowing of the current profile is accompanied by a transient increase in the internal toroidal magnetic field, B_{Ti} (Fig. 3e). The toroidal field B_{Ti} and its associated poloidal currents, J_P, are self-generated by the plasma in order to achieve a force-free state. Given that both the laboratory and solar flux ropes are magnetically rather than thermally dominated, the measured B_{Ti} is paramagnetic in nature (that is, it enhances rather than cancels the ambient guide field, B_g). As such, the poloidal currents, J_P, cross with the toroidal field, B_T, to produce a large, dynamic tension force that causes the eruption to fail (see Methods).

In the absence of substantial B_g, the tension force is much reduced. This leads to the eruptive behaviour shown in Extended Data Fig. 3, where the J_T profile remains relatively uniform throughout the event and the flux rope expands freely towards the wall of the machine. The observed rapid reformation of the flux rope after the eruption may differ from events in the solar corona. Assessing the impact of laboratory factors such as external inductance and boundary conditions on this phenomenon is an important topic for future work.

As a final step, we now quantitatively examine the magnetic forces acting on the flux rope. The three forces considered here are the hoop (F_h), strapping (F_s), and toroidal field tension (F_t) terms (see Methods and Extended Data Table 3). For the failed torus event in Fig. 3, all three force terms initially decline in magnitude (see Fig. 3c). As the event proceeds, however, the tension force dramatically surges in magnitude, thereby halting the upward motion of the flux rope. For the eruptive event in Extended Data Fig. 3, on the other hand, all three force terms decline monotonically. The remarkable transient increase of the tension force in the failed event warrants further investigation. Figure 3b shows that there is a rapid conversion of poloidal to toroidal magnetic flux during the failed torus event. This flux conversion is the signature of a dynamic plasma relaxation event such as those observed in laboratory fusion devices[29].

Relaxation events occur because the plasma can find a lower energy state through internal reconfiguration rather than through external eruption. The traditional view is that the system 'self-organizes' to a lower energy state while conserving magnetic helicity, and that the underlying physical mechanism is magnetic reconnection[30]. This reconnection is transient, three-dimensional, and internal to the flux rope, making it difficult to track experimentally. Nonetheless, the plasma's tendency to conserve helicity sheds light on the observed behaviour. Helicity characterizes the linkage between the poloidal and toroidal fluxes such that the product of the two is approximately conserved. Thus, the hollowing of the J_T profile, which reduces the poloidal flux in the rope, must be accompanied by a surge in the toroidal flux (and therefore a surge in the toroidal field tension force). Finally, we observe relaxation events only when the potential guide field is large enough to prevent the flux rope from kinking (that is, $q_a \gtrsim 0.8$). When $q_a \lesssim 0.8$, on the other hand, self-organization fails because of the disruptive nature of the external kink mode.

With the laboratory results in hand, we now turn to their implications for eruptions in the solar corona. First, the existence of the failed torus regime implies that the onset of the torus instability is not a sufficient condition for eruption. As such, the toroidal field tension force that produces failed torus events must be added to the physical models that are used to study solar eruptions. Doing so presents a substantial challenge for two reasons.

First, because the toroidal field tension force dynamically surges during a failed torus event, time-resolved modelling of the flux rope is crucial. This rules out quasi-static nonlinear force-free field (NLFFF) modelling, which has shown promise as a tool for understanding coronal configurations such as erupting sigmoids[14]. Second, the plasma relaxation events that enhance the toroidal field tension force are inherently three-dimensional[29]. As such, the full line-tied geometry of the flux rope must be modelled in both time and space in order to resolve the physical mechanisms that define the failed torus regime. These difficult modelling requirements may explain why this regime has not been previously identified in numerical simulations.

Our results also have direct implications for remote observations of the corona. For example, the presence of a substantial guide magnetic field in the potential field configuration of a given flux rope should indicate a reduced probability of eruption. This information can be obtained from relatively simple reconstructions of the flux rope's magnetic topology, even if a full model of the dynamically evolving magnetic field is not available. One promising candidate for study is the recent non-eruptive active region of the Sun's surface NOAA AR 12192, which was one of the largest and longest-lived active regions of the space age. This region produced multiple large flares (it was the most prolific active region in solar cycle 24), but no coronal mass ejections were observed during its disk passage[15]. Preliminary inspection of the observational data shows that a number of the flares were associated with failed eruptions in the torus-unstable regime. If these events were indeed failed torus events, they may be explained by the toroidal field tension force mechanism identified here.

Finally, our results do not preclude the torus instability as an eruption mechanism for kink-stable flux ropes. Rather, they demonstrate that torus-driven eruptions can fail under certain conditions. Thus, comparing and contrasting the features of kink-stable flux ropes that do erupt with those that fail is a key next step towards a comprehensive understanding of the flux rope instability parameter space.

References

1. Kunow, H., Crooker, N. U., Linker, J. A., Schwenn, R. & von Steiger, R. (eds.) *Coronal Mass Ejections* (Springer, 2006). Ch. 2, 12.

2. Kuperus, M. & Raadu, M. A. The support of prominences formed in neutral sheets. *Astron. Astrophys.* **31**, 189–193 (1974).

3. Chen, J. Effects of toroidal forces in current loops embedded in a background plasma. *Astrophys. J.* **338**, 453–470 (1989).

4. Titov, V. S. & Démoulin, P. Basic topology of twisted magnetic configurations in solar flares. *Astron. Astrophys.* **351**, 707–720 (1999).

5. Amari, T., Canou, A. & Aly, J.-J. Characterizing and predicting the magnetic environment leading to solar eruptions. *Nature* **514**, 465–469 (2014).

6. Ji, H., Wang, H., Schmahl, E. J., Moon, Y.-J. & Jiang, Y. Observations of the failed eruption of a filament. *Astrophys. J. Lett.* **595**, L135–L138 (2003).

7. Török, T. & Kliem, B. Confined and ejective eruptions of kink-unstable flux ropes. *Astrophys. J.* **630**, L97–L100 (2005).

8. Joshi, N. C. *et al.* Confined partial filament eruption and its reformation within a stable magnetic flux rope. *Astrophys. J.* **787**, 11 (2014).

9. Forbes, T. G. & Isenberg, P. A. A catastrophe mechanism for coronal mass ejections. *Astrophys. J.* **373**, 294–307 (1991).

10. Kliem, B. & Török, T. Torus instability. *Phys. Rev. Lett.* **96**, 255002 (2006).

11. Fan, Y. & Gibson, S. E. Onset of coronal mass ejections due to loss of confinement of coronal flux ropes. *Astrophys. J.* **668**, 1232–1245 (2007).

12. Liu, Y. Magnetic field overlying solar eruption regions and kink and torus instabilities. *Astrophys. J. Lett.* **679**, L151–L154 (2008).

13. Démoulin, P. & Aulanier, G. Criteria for flux rope eruption: Non-equilibrium versus torus instability. *Astrophys. J.* **718**, 1388–1399 (2010).

14. Savcheva, A., Pariat, E., van Ballegooijen, A., Aulanier, G. & DeLuca, E. Sigmoidal active region on the sun: Comparison of a magnetohydrodynamical simulation and a nonlinear force-free field model. *Astrophys. J.* **750**, 15 (2012).

15. Sun, X. *et al.* Why is the great solar active region 12192 flare-rich but CME-poor? *Astrophys. J. Lett.* **804**, L28 (2015).

16. Myers, C. E. *Laboratory Study of the Equilibrium and Eruption of Line-Tied Magnetic Flux Ropes in the Solar Corona*. Ph.D. thesis, Princeton University (2015). URL `http://arks.princeton.edu/ark:/88435/dsp01dv13zw44b`.

17. Hansen, J. F. & Bellan, P. M. Experimental demonstration of how strapping fields can inhibit solar prominence eruptions. *Astrophys. J.* **563**, L183–L186 (2001).

18. Soltwisch, H. *et al.* Flarelab: Early results. *Plasma Phys. Control. Fusion* **52**, 124030 (2010).

19. Tripathi, S. K. P. & Gekelman, W. Laboratory simulation of arched magnetic flux rope eruptions in the solar atmosphere. *Phys. Rev. Lett.* **105**, 075005 (2010).

20. Gold, T. & Hoyle, F. On the origin of solar flares. *Mon. Not. R. Astron. Soc.* **120**, 89–105 (1960).

21. Sakurai, T. Magnetohydrodynamic interpretation of the motion of prominences. *Publ. Astron. Soc. Japan* **28**, 177–198 (1976).

22. Hood, A. W. & Priest, E. R. Critical conditions for magnetic instabilities in force-free coronal loops. *Geophys. Astrophys. Fluid Dyn.* **17**, 297–318 (1981).

23. Mikić, Z., Schnack, D. D. & van Hoven, G. Dynamical evolution of twisted magnetic flux tubes. I – Equilibrium and linear stability. *Astrophys. J.* **361**, 690–700 (1990).

24. T. Török, B. Kliem & V. S. Titov. Ideal kink instability of a magnetic loop equilibrium. *Astron. Astrophys.* **413**, L27–L30 (2004).

25. Kruskal, M. & Schwarzschild, M. Some instabilities of a completely ionized plasma. *Proc. R. Soc. Lond. A* **223**, 348–360 (1954).

26. Shafranov, V. The stability of a cylindrical gaseous conductor in a magnetic field. *Sov. J. At. Energy* **1**, 709–713 (1956).

27. Ryutov, D. D., Furno, I., Intrator, T. P., Abbate, S. & Madziwa-Nussinov, T. Phenomenological theory of the kink instability in a slender plasma column. *Phys. Plasmas* **13**, 032105 (2006).

28. Olmedo, O. & Zhang, J. Partial torus instability. *Astrophys. J.* **718**, 433–440 (2010).

29. Ji, H., Prager, S. C. & Sarff, J. S. Conservation of magnetic helicity during plasma relaxation. *Phys. Rev. Lett.* **74**, 2945–2948 (1995).

30. Taylor, J. B. Relaxation and magnetic reconnection in plasmas. *Rev. Mod. Phys.* **58**, 741–763 (1986).

Acknowledgements We thank R. Cutler for constructing the flux rope experiment and for myriad technical contributions. We also thank F. Scotti and P. Sloboda for additional technical contributions and R. M. Kulsrud for theoretical discussions. This research is supported by Department of Energy (DoE) Contract No. DE-AC02-09CH11466 and by the National Science Foundation/DoE Center for Magnetic Self-Organization (CMSO).

Author Contributions C.E.M., M.Y., and H.J. designed the laboratory experiments. C.E.M., J.Y., and J.J.-A. carried out the experiments and processed the data. C.E.M., M.Y., H.J., J.Y., W.F., and J.J.-A. interpreted the laboratory results. A.S. and E.E.DeL. placed the laboratory results in the context of solar observations and modelling. C.E.M. analysed the laboratory data, prepared the figures, and wrote the manuscript. All authors contributed to the revision of the manuscript.

Author Information The digital data for this paper can be found at `http://arks.princeton.edu/ark:/88435/dsp01j3860933c`. Reprints and permissions information is available at `www.nature.com/reprints`. The authors declare no competing financial interests. Readers are welcome to comment on the online version of the paper. Correspondence and requests for materials should be addressed to C.E.M. (cmyers@pppl.gov).

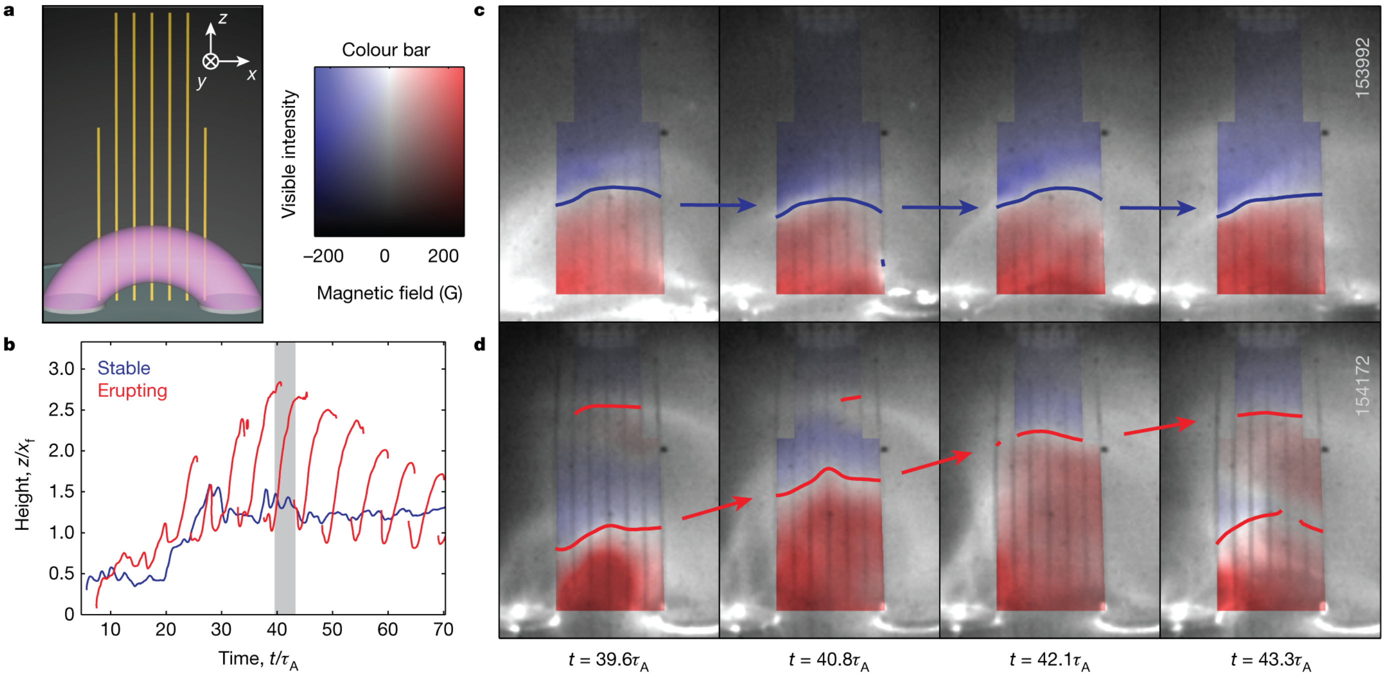

Figure 1 | Representative stable and erupting flux rope discharges. **a**, Experimental setup showing the arched flux rope (pink) attached to two conducting footpoints. The yellow vertical lines represent the *in situ* magnetic probes (see Methods). **b**, Height-time histories of the two flux rope discharges. The frame sequences in **c** and **d** are taken from the short time period shaded in grey. **c**, **d**, Frame sequences with the measured out-of-plane magnetic field overlaid on corresponding fast camera visible light images (data ID numbers are shown on the right). The measured magnetic axis locations (the solid lines) are defined by the reversal of the out-of-plane magnetic field (see Methods). A video of the full discharge evolution is included as a Supplemental Video. τ_A, dynamic Alfvén time; x_f, footpoint separation distance; z, vertical height above the footpoints.

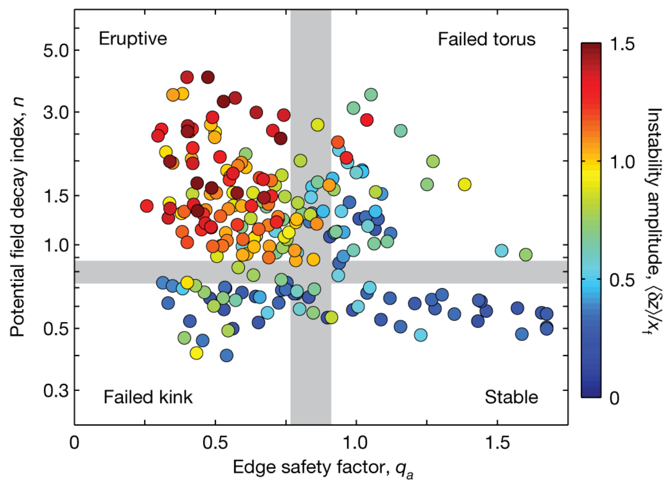

Figure 2 | The experimentally measured torus versus kink instability parameter space. The x axis represents the kink instability through the edge safety factor q_a (the inverse magnetic twist), while the y axis represents the torus instability through the potential field decay index n. Each data point is the mean of 2–5 flux rope plasma discharges with the same experimental parameters. A total of 806 flux rope plasma discharges are represented. The metric used here to quantify the eruptivity of each flux rope is the normalized spatial instability amplitude $\langle \delta z \rangle / x_f$ (see Methods). A value of $\langle \delta z \rangle / x_f < 0.5$ is stable, while $\langle \delta z \rangle / x_f > 1$ is clearly eruptive. The shaded boundaries, which are empirically identified, delineate the four distinct instability parameter regimes described in the text.

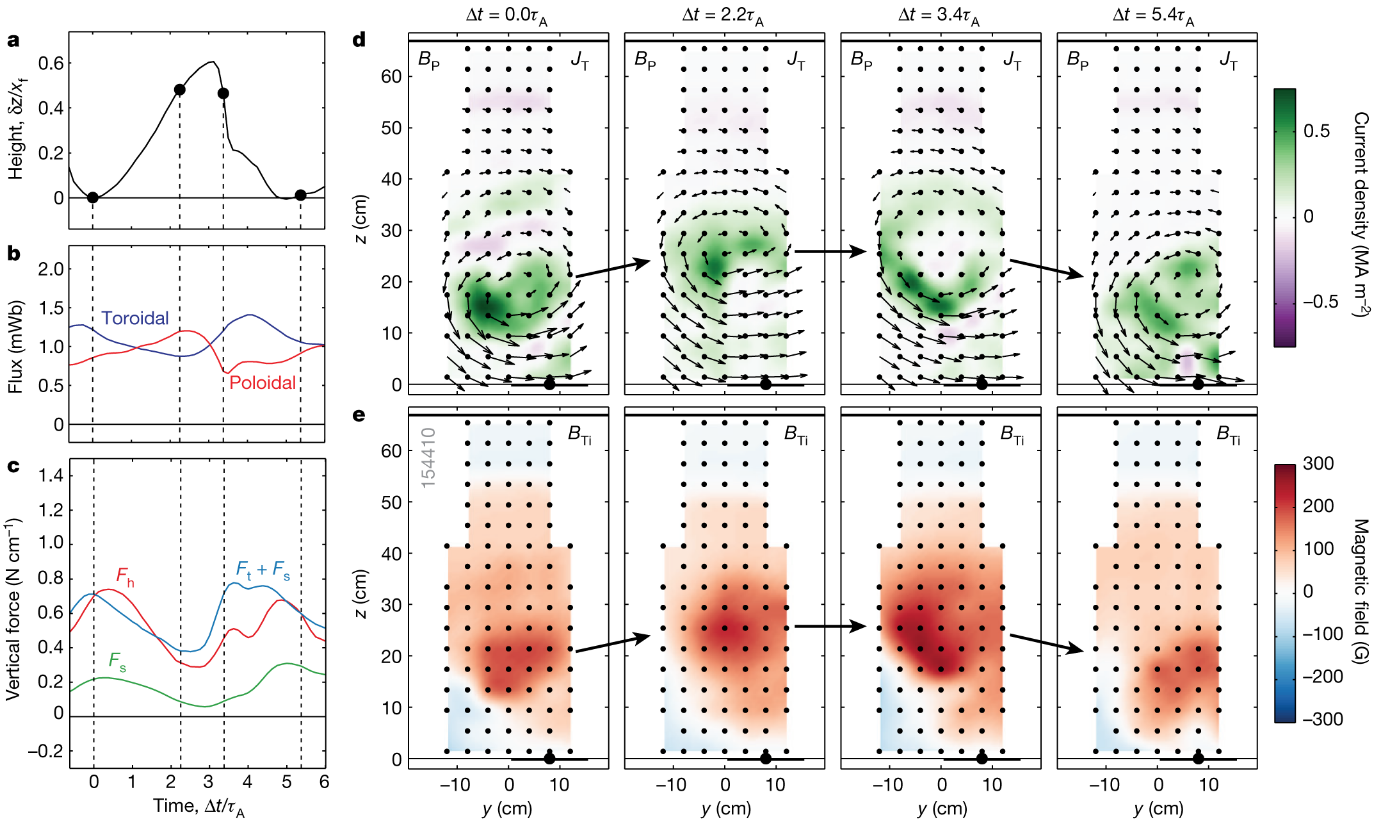

Figure 3 | Magnetic analysis of a characteristic failed torus event. See Extended Data Fig. 4b for the magnetic probe orientation. **a**, Relative perturbation amplitude showing that the flux rope initially expands before collapsing back downward. **b**, Time evolution of the toroidal and poloidal magnetic fluxes within the flux rope. **c**, Time evolution of the hoop (F_h), strapping (F_s), and toroidal field tension (F_t) forces, showing the surge in the tension force that ultimately causes the event to fail. **d**, **e**, Sequenced spatial plots of the toroidal current density (J_T) and the internal toroidal field (B_{Ti}) showing the dramatic hollowing of J_T and the simultaneous transient increase in B_{Ti} (compare with Extended Data Fig. 3).

Methods

Candidate solar eruption mechanisms

Ideal magnetohydrodynamic instabilities such as the torus and kink instabilities are central to the standard storage-and-release model of solar flares and coronal mass ejections[1]. In addition to such ideal instabilities, the non-ideal process of magnetic reconnection is routinely invoked to explain various observed solar flare and coronal mass ejection features. For example, reconnection produces flare emission beneath the expanding/rising flux rope and contributes to the evolution of the flux rope height[31]. Reconnection is also the central driving mechanism in some coronal mass ejection initiation models[32]. Magnetohydrodynamic simulations and data-driven modelling have shown, however, that the torus instability plays a crucial part in driving magnetic flux ropes to erupt, even in the presence of magnetic reconnection[14]. Accordingly, our flux rope experiments are designed to identify the stability boundaries for the triggering of candidate ideal instability eruption mechanisms.

The torus instability is triggered by an imbalance in the vertical forces acting on the flux rope plasma[10]. The traditional forces considered for the torus instability are (1) the upward 'hoop' force F_h, which is the Lorentz force between the toroidal (axial) flux rope current and its own poloidal (azimuthal) magnetic field; and (2) the downward 'strapping' force F_s, which is the Lorentz force between the same toroidal current and the potential strapping field (see the Methods subsection 'Magnetic force analysis'). Analysis of Shafranov's toroidal equilibrium equations[33] reveals that the torus instability threshold can be expressed analytically in terms of the potential field 'decay index'[10, 34]:

$$n(z) = -\frac{z}{|\mathbf{B}_{pot}|}\frac{\partial |\mathbf{B}_{pot}|}{\partial z}, \tag{1}$$

where $\mathbf{B}_{pot}$ is the potential magnetic field and z is the height above the solar surface. A larger value of n indicates a more quickly decaying potential field. For a toroidally symmetric, large-aspect-ratio flux rope, the torus instability criterion[10, 34] reduces to $n \geq 3/2$, which is a remarkably concise result given the complexity of the system. Much effort has been expended to more accurately determine the torus threshold for the realistic line-tied conditions of the solar corona, but a wide range of estimates remain[13, 16, 28, 35].

The kink instability[20–24], on the other hand, is triggered when the twist in the magnetic field at the edge of the flux rope (that is, the poloidal angle through which an edge magnetic field line rotates as it transits the toroidal length of the flux rope) exceeds a critical threshold[25, 26]. The analytical kink onset condition is often given in terms of the edge safety factor[25–27], q_a, which is defined as the inverse of the edge magnetic twist, ι_a:

$$q_a \equiv \frac{2\pi}{\iota_a} = \left.\frac{d\Phi_T}{d\psi_P}\right|_{r=a} \simeq \frac{2\pi a}{L}\frac{B_{Ta}}{B_{Pa}}. \tag{2}$$

Here, Φ_T is the enclosed toroidal magnetic flux, ψ_P is the enclosed poloidal magnetic flux, r is the minor radial coordinate, and a is the minor radius of the flux rope. In the latter expression, L is the rope length, B_{Ta} is the edge toroidal field strength, and B_{Pa} is the edge poloidal field strength. The well-known Kruskal-Shafranov kink criterion[25–27] predicts instability for $q_a \leq 1$, but numerical analyses of arched, line-tied flux ropes at finite aspect ratio[22, 24] have predicted a more stable criterion of $q_a \lesssim 0.8$. Previous laboratory experiments on linear[36–38] and arched[39] line-tied flux ropes have demonstrated the importance of the line-tied boundary conditions to the kink stability criterion. In spite of these efforts, the combined stability against both torus and kink perturbations in the two-dimensional n versus q_a parameter space has not been well explored.

Experimental setup and solar relevance

Our experiments are conducted in the Magnetic Reconnection Experiment (MRX)[40] at Princeton Plasma Physics Laboratory. To produce solar-relevant line-tied magnetic flux ropes, the MRX device is substantially modified from its standard operating mode[16]. In particular, its magnetic-reconnection-producing 'flux cores' are removed and replaced with a custom-built flux rope apparatus that contains the following: (1) two electrodes that serve as the flux rope footpoints; (2) two sets of magnetic field coils inside the vessel that produce the guide and strapping potential magnetic field; and (3) a glass substrate that physically separates the $z > 0$ plasma region from the $z < 0$ field coil region (see Extended Data Fig. 1). The two electrodes are circular copper discs with a footpoint radius of $a_f \simeq 7.5$ cm and a horizontal separation distance of $2x_f \simeq 36$ cm. The entire flux rope apparatus is housed within a cylindrical stainless steel vacuum vessel that is evacuated to $p \sim 10^{-6}$ Torr. Finally, two additional sets of magnetic field coils located outside the vessel are used to adjust the guide and strapping field spatial profiles.

Before a flux rope plasma can be produced in the experiment, the desired potential magnetic field configuration must be created. This is accomplished by energizing the four independent magnetic field coil sets introduced above. Each potential field component (guide or strapping) is produced by superposing the fields from two of the four available coil sets (one inside the vessel and one outside the vessel per field component). This superposition provides two degrees of freedom for each field component that are typically used to independently set the field strength and the field decay index (see equation (1)). The independent control of these two parameters for both the guide and strapping fields facilitates a systematic exploration of the torus versus kink instability parameter space.

Once a given potential field configuration has been selected, a precisely timed sequence of events is initiated. First, the potential magnetic field coils are energized to their requested settings and held there for the duration of the discharge. In practice, the potential field ramp is completed 7 ms prior to the formation of the flux rope plasma. This is more than twice the inductive skin time of the vessel wall and of the copper electrodes ($\tau_w \sim \tau_f \sim 3$ ms), such that any induced eddy currents decay away before the plasma is formed. Next, neutral gas, typically hydrogen, is injected into the vessel to provide a particle source for the plasma. The gas is injected at both the vessel wall and directly at the cathode surface in order to ensure consistent plasma breakdown at reasonable fill pressures and firing voltages ($p \sim 10$ mTorr, $V \sim 4$ kV). Finally, a charged capacitor bank is connected across the electrodes to break down the neutral gas into an arc discharge plasma. As electric current and therefore free magnetic energy is slowly injected into the system, the pre-existing potential magnetic field lines are twisted into a magnetic flux rope. This procedure is repeated thousands of times over the course of the experimental campaign in order to generate flux ropes with a wide range of equilibrium and stability properties.

The typical parameters of our laboratory flux ropes are displayed in Extended Data Table 1. These laboratory parameters can be used to compute key dimensionless physics parameters that justify the relevance of our laboratory experiments to storage-and-release eruptions in the solar corona (see Extended Data Table 2). First, a strict timescale ordering must be satisfied. In particular, the aforementioned driving timescale, τ_D, must be substantially longer than the dynamic Alfvén timescale, τ_A, and substantially shorter than the resistive timescale, τ_R. The separation between τ_A and τ_D satisfies the storage-and-release requirement, while the separation between τ_D and τ_R respects the high conductivity of the solar corona.

Additionally, for the physical phenomena observed in the laboratory to be independent of scale (and therefore be applicable to the corona), the laboratory plasma must reside in the magnetohydrodynamic regime. Such extrapolation is possible because magnetohydrodynamics has no fundamental spatial length scale[41]. The magnetohydrodynamic nature of a given plasma is characterized by the remaining parameters in Extended Data Table 2. First, $\rho_i/a \ll 1$ indicates that the ratio of the Larmor radius of individual ions to the flux rope minor radius is small, such that scale-dependent finite Larmor radius effects are negligible. Second, $\lambda_{ei}/L \ll 1$ indicates that the plasma collisionality is high, such that the fluid approximation employed by magnetodynamics is valid. Third, the Lundquist Number $S \gg 1$ is large, such that magnetic field lines are frozen into the plasma and ideal magnetohydromic instabilities such as the kink and torus instabilities will govern the behaviour of the system. Fourth, the ionization fraction, $n_e/(n_e + n_n)$, indicates that the laboratory plasma is ionized sufficiently for magnetodynamic rather than neutral physics to dominate. Finally, the plasma $\beta \ll 1$ indicates that the plasma is magnetically rather than thermally dominated. This combination of dimensionless parameters justifies the application of our laboratory experiments to the solar eruption problem.

Laboratory diagnostics

Two primary diagnostics are used in our experiments: fast visible light cameras and *in situ* magnetic probes. Data from both diagnostics are compared in Fig. 1. The fast cameras are used to qualitatively assess the location and performance of the arc discharge plasmas. They are Vision Research Phantom v710 monochrome cameras operated with a 1-μs exposure at 270,000 frames per second (~ 3-μs, 1-τ_A cadence). The collected light spans the visible spectrum, with the primary contribution coming from the Hα hydrogen neutral line. The dominance of neutral light in these images makes them fundamentally different from the extreme-ultraviolet images of the solar corona that are acquired by instruments such as the Atmospheric Imaging Assembly (AIA) aboard the Solar Dynamics Observatory (SDO)[42].

The *in situ* magnetic probes, on the other hand, directly measure the internal magnetic structure of the flux rope plasma. Each probe is constructed from a long, thin glass tube (64 cm long, 0.7 cm diameter) that houses up to 51 miniature magnetic pickup coils that are distributed along its length. These pickup coils each measure the time derivative of one component of the vector magnetic field, and the resulting signals are integrated to measure the magnetic field as a function of time. The pickup coils are grouped in orthogonal triplets in order to measure the complete vector field at each spatially distributed location. Seven such probes housing approximately 300 total pickup coils are inserted into the plasma in order to map out the magnetic field at more than 100 locations in a two-dimensional plane. The triplets within each probe are separated vertically at 4 cm intervals, and the seven probes are separated horizontally by 4 cm to produce a 4 cm $\times$ 4 cm measurement grid over a 24 cm $\times$ 64 cm cross-section of the plasma. As shown in Extended Data Fig. 4, this two-dimensional plane can be oriented parallel to or orthogonal to the flux rope axis. Sample magnetic field measurements for each case are also shown, with the colour representing the out-of-plane field and the vectors representing the in-plane field. Both the arched shape of the flux rope and its quasi-circular cross-section are clearly visible in these data. The magnetic field data is digitized at 2.5 MHz (0.4-μs, 0.1-τ_A timebase). As such, the instabilities studied here are well resolved temporally. Though the magnetic probes are inserted directly into the plasma, they are thin and non-conducting and therefore largely non-perturbative. Their use in MRX for detailed physics studies is well established[43].

Height-time evolution and instability parameter space analysis

To characterize the behaviour of a given flux rope plasma, the spatially distributed magnetic field data acquired during the discharge can be reduced to a 'height-time' plot that succinctly tracks the evolution of the flux rope magnetic axis. This is accomplished by selecting a single vertical magnetic probe from the array and extracting the measured $B_y(t, z)$ data. The B_y field component is the superposition of the 'internal' poloidal field produced by the plasma, B_{Pi}, and the external strapping field, B_s. Its reversal point at $B_y(t, z) = 0$ therefore constitutes a measurement of the magnetic axis of the flux rope. Four sample height-time plots, one from each of the four instability regimes identified in Fig. 2, are shown in Extended Data Fig. 5. The colour in each height-time plot represents $B_y(t, z)$, with the black line indicating the measured magnetic axis location. The qualitative differences between the different instability regimes are clearly visible in these plots. To arrive at the more quantitative assessment of the instability parameter space presented in Fig. 2, however, the height-time data must be further reduced.

In our experiments, we use three scalar quantities to summarize the performance of a given flux rope plasma: (1) the edge safety factor, q_a; (2) the field decay index, n; and (3) the spatial instability amplitude, $\langle \delta z \rangle / x_f$. The first two parameters place the plasma within the torus versus kink instability parameter space, while the third is a metric developed to quantify the eruptivity of a given flux rope. In each discharge, q_a and n are evaluated at the maximum of the $\langle z_{apex} \rangle$ waveform, which tracks the time-averaged height of the flux rope apex (see Extended Data Fig. 5). The evaluation of n via equation (1) is straightforward given that the potential field magnitude, $|\mathbf{B}_{pot}|$, is well-defined by the geometry of the magnetic field coils in the experiment.

To evaluate $q_a \simeq 2\pi a B_{Ta}/L B_{Pa}$ via equation (2), on the other hand, the footpoint values of the minor radius and the magnetic fields are used: $a = a_f$, $B_{Ta} = B_{gf}$, and $B_{Pa} = B_{Pf} \simeq \mu_0 I_T / 2\pi a_f$, where I_T is the toroidal flux rope current. The length of the rope, L, is approximated here using a 'shifted-circle' model for the rope axis[3,16] that depends only on the apex height, $\langle z_{apex} \rangle$, and the footpoint separation distance, x_f. This approximation for q_a assumes that toroidal flux is conserved along the length of the flux rope. It can have errors of up to 10%, however, which are mostly caused by uncertainty in the fraction of the measured capacitor bank current that is carried in the flux rope. Based on magnetic probe measurements, this fraction is typically 90%. The final step is to evaluate the instability amplitude metric, $\langle\delta z\rangle/x_f$. Here, the dynamic spatial amplitude $\langle\delta z\rangle$ is defined as the maximum of the envelope of the dynamic motion of the magnetic axis. The relevant values of q_a, n, and $\langle\delta z\rangle/x_f$ are listed in Extended Data Fig. 5c. These values show that the instability amplitude provides a quantitative assessment of the qualitatively disparate behaviours of the four flux rope discharges in Extended Data Fig. 5b. Finally, in order to produce the parameter space scatterplot in Fig. 2, the data from multiple flux rope plasmas with the same experimental parameters are combined. Each data point in Fig. 2 contains the mean of 2–5 discharges such that more than 800 discharges are represented.

Magnetic force analysis

The magnetic probe data are also used to directly measure the magnetic forces acting on the line-tied flux rope. These force measurements are used to demonstrate the key role of the toroidal field tension force in the failed torus regime. The forces in a low-β plasma (one with negligible thermal pressure) are dominated by magnetic $\mathbf{J}\times\mathbf{B}$ Lorentz forces, where $\mathbf{J}$ is the current density and $\mathbf{B}$ is the magnetic field. Here, the total force density $\mathbf{J}\times\mathbf{B}$ is decomposed into three key contributions: (1) the hoop force, F_h; (2) the strapping force, F_s; and (3) the tension force, F_t (see Extended Data Table 3). The hoop force pushes the flux rope plasma outward, while the strapping and tension forces push downward and work together to confine the rope.

The first step in evaluating the three force terms described above is to decompose the magnetic field and current density into the individual components that contribute to each force term (see Extended Data Table 3). Sample magnetic field and current density measurements are shown in Extended Data Fig. 6. The computation of J_P from the B_{Ti} data requires a measurement of the toroidal curvature of the rope (see below). The final output of the field and force decomposition in Extended Data Table 3 is the set of force densities f_h, f_s, and f_t. These quantities are 'force densities' rather than forces because they have units of force per volume. The forces plotted in Fig. 3 and Extended Data Fig. 3, on the other hand, are the forces per unit length, F_h, F_s, and F_t, that are integrated from the aforementioned force density terms. It is important to note that the tension force density, f_t, actually contains both magnetic tension and pressure contributions. The tension contribution is derived from the toroidal curvature of the magnetic field in the arched flux rope, and at large aspect ratio its leading term is proportional to $B_{Ti}B_T/R$, where R is the radius of curvature of the flux rope[16]. The pressure contribution, on the other hand, is derived from gradients in the internal toroidal field, B_{Ti}. In practice, the tension contribution to f_t dominates the pressure contribution. As such, here we refer to f_t as simply the toroidal field tension force to avoid unnecessarily complicating the physics discussion.

As noted above, the force densities must be integrated above over the cross-section of the flux rope. This converts the force densities, f, to the forces per unit length, F, that are plotted in Fig. 3c and Extended Data Fig. 3c. The cross-section integral takes the form:

$$F(z_{apex}) = \frac{1}{R_{apex}} \int_0^{2\pi} d\theta \int_0^a dr \left[r\, h_T(z)\, f(r,\theta) \right], \tag{3}$$

where R_{apex} is the radius of curvature at the flux rope apex, (r, θ) are cylindrical coordinates in the (y, z) plane, $a(\theta)$ is the flux rope minor radius, and h_T is the toroidal curvilinear scale factor that accounts for the toroidal curvature of the flux rope. The curvilinear scale factor is directly measured from flux rope plasmas with the probe array aligned in the toroidal cross-section (see Extended Data Fig. 4). The resulting curvature measurements are then used to analyse the magnetic forces in equivalent flux rope plasmas with the probe array aligned in the poloidal cross-section[16]. The remaining quantity in equation (3) is the minor radius $a(\theta)$, which sets the extent of the flux rope cross-section. This quantity is obtained via the poloidal flux function of the flux rope $\psi(y, z)$. The flux function is obtained by line integrating the measured poloidal magnetic field components as follows:

$$\psi(y,z) = -\int_{C_y} dy\; h_T B_z + \int_{C_z} dz\; h_T B_y, \tag{4}$$

where B_y and B_z are the in-plane components of the poloidal field and C_y and C_z are the paths of integration along each direction. By construction, the integration is path independent. Contours of the resulting poloidal flux function are shown in blue on the left-hand side of Extended Data Fig. 6. The minor radius $a(\theta)$, shown in red, is defined by the flux function contour that encloses $\sim 90\%$ of the total current that is fed to the electrodes. With the minor radius now defined, the three forces per unit length can be computed at each instant in time. These integration techniques are also used to evaluate the toroidal and poloidal magnetic fluxes that are plotted in Fig. 3 and Extended Data Fig. 3. An extensive analysis of the equilibrium force balance in non-erupting flux ropes benchmarks the strapping force measured with these techniques to within 5% of analytical expectations. Furthermore, a force-free equilibrium is measured to within $\pm 15\%$ of the hoop force magnitude[16] over an ensemble of hundreds of non-erupting flux ropes. These results give confidence in the force measurements presented in Fig. 3 and Extended Data Fig. 3.

Methods References

31. Moore, R. L., Sterling, A. C., Hudson, H. S. & Lemen, J. R. Onset of the magnetic explosion in solar flares and coronal mass ejections. *Astrophys. J.* **552**, 833–848 (2001).

32. Antiochos, S. K., DeVore, C. R. & Klimchuk, J. A. A model for solar coronal mass ejections. *Astrophys. J.* **510**, 485–493 (1999).

33. Shafranov, V. Plasma equilibrium in a magnetic field. In Leontovich, M. A. (ed.) *Reviews of Plasma Physics*, vol. 2, 103–152 (Consultants Bureau Enterprises, New York, 1966).

34. Bateman, G. *MHD Instabilities* (MIT Press, 1978).

35. Kliem, B., Lin, J., Forbes, T. G., Priest, E. R. & Török, T. Catastrophe versus instability for the eruption of a toroidal solar magnetic flux rope. *Astrophys. J.* **789**, 46 (2014).

36. Hsu, S. C. & Bellan, P. M. Experimental identification of the kink instability as a poloidal flux amplification mechanism for coaxial gun spheromak formation. *Phys. Rev. Lett.* **90**, 215002 (2003).

37. Furno, I., Intrator, T. P., Ryutov, D. D., Abbate, S. *et al.* Current-driven rotating-kink mode in a plasma column with a non-line-tied free end. *Phys. Rev. Lett.* **97**, 015002 (2006).

38. Bergerson, W. F., Forest, C. B., Fiksel, G., Hannum, D. A. *et al.* Onset and saturation of the kink instability in a current-carrying line-tied plasma. *Phys. Rev. Lett.* **96**, 015004 (2006).

39. Oz, E. *et al.* Experimental verification of the Kruskal-Shafranov stability limit in line-tied partial-toroidal plasmas. *Phys. Plasmas* **18**, 102107 (2011).

40. Yamada, M. *et al.* Study of driven magnetic reconnection in a laboratory plasma. *Phys. Plasmas* **4**, 1936–1944 (1997).

41. Bellan, P. M. & Hansen, J. F. Laboratory simulations of solar prominence eruptions. *Phys. Plasmas* **5**, 1991–2000 (1998).

42. Lemen, J. R. *et al.* The Atmospheric Imaging Assembly (AIA) on the Solar Dynamics Observatory (SDO). *Solar Phys.* **275**, 17–40 (2012).

43. Yoo, J., Yamada, M., Ji, H. & Myers, C. E. Observation of ion acceleration and heating during collisionless magnetic reconnection in a laboratory plasma. *Phys. Rev. Lett.* **110**, 215007 (2013).

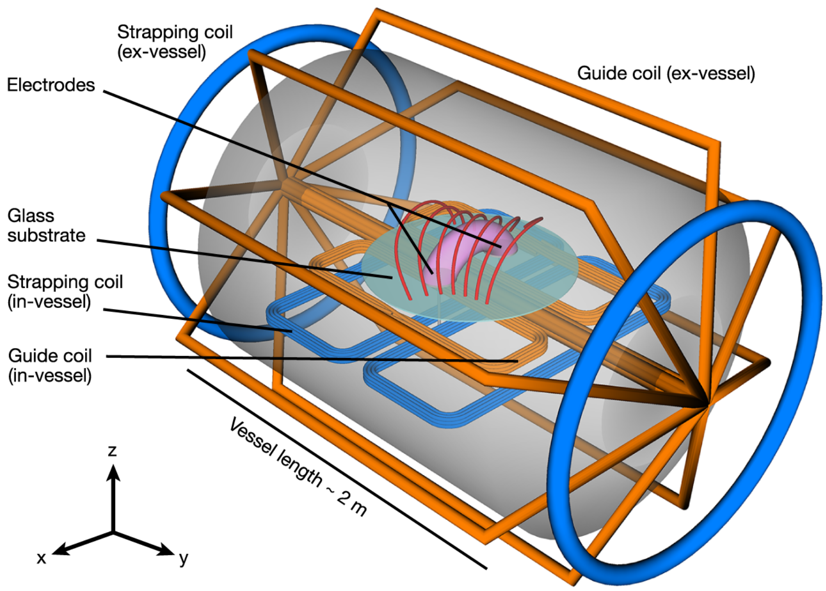

Extended Data Figure 1 | Experimental setup. A plasma arc (pink) is maintained between two electrodes that are mounted on a glass substrate. The electrodes, which serve as the flux rope footpoints, are horizontally separated by $2x_f = 36$ cm, and they have a minor radius of $a_f = 7.5$ cm. The vertical distance from these footpoints to the vessel wall is $z_w \sim 70$ cm. Four magnetic field coil sets (two inside the vessel, two outside) work in concert to produce a variety of potential magnetic field configurations. More specifically, the two orange coil sets are used to produce the guide potential field, while the two blue coil sets are used to produce the strapping potential field.

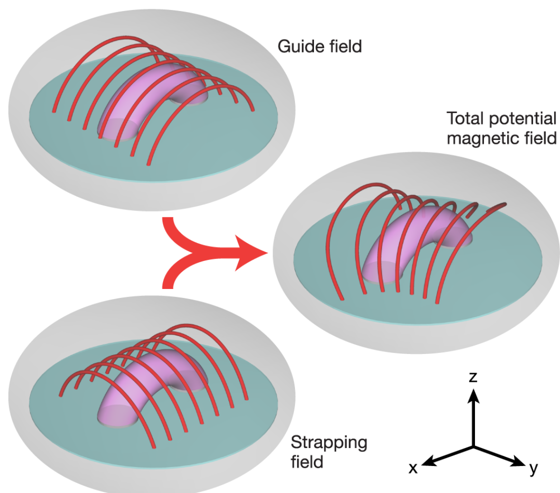

Extended Data Figure 2 | Components of the potential magnetic field configuration. The strapping field runs perpendicular to the flux rope axis and produces the well-known strapping force whose rapid decay can trigger the torus instability. The guide field, on the other hand, runs toroidally along the flux rope axis. It stabilizes the kink instability and generates a confining magnetic tension force. The total potential magnetic field, which is the superposition of the guide and strapping field contributions, is obliquely aligned to the flux rope.

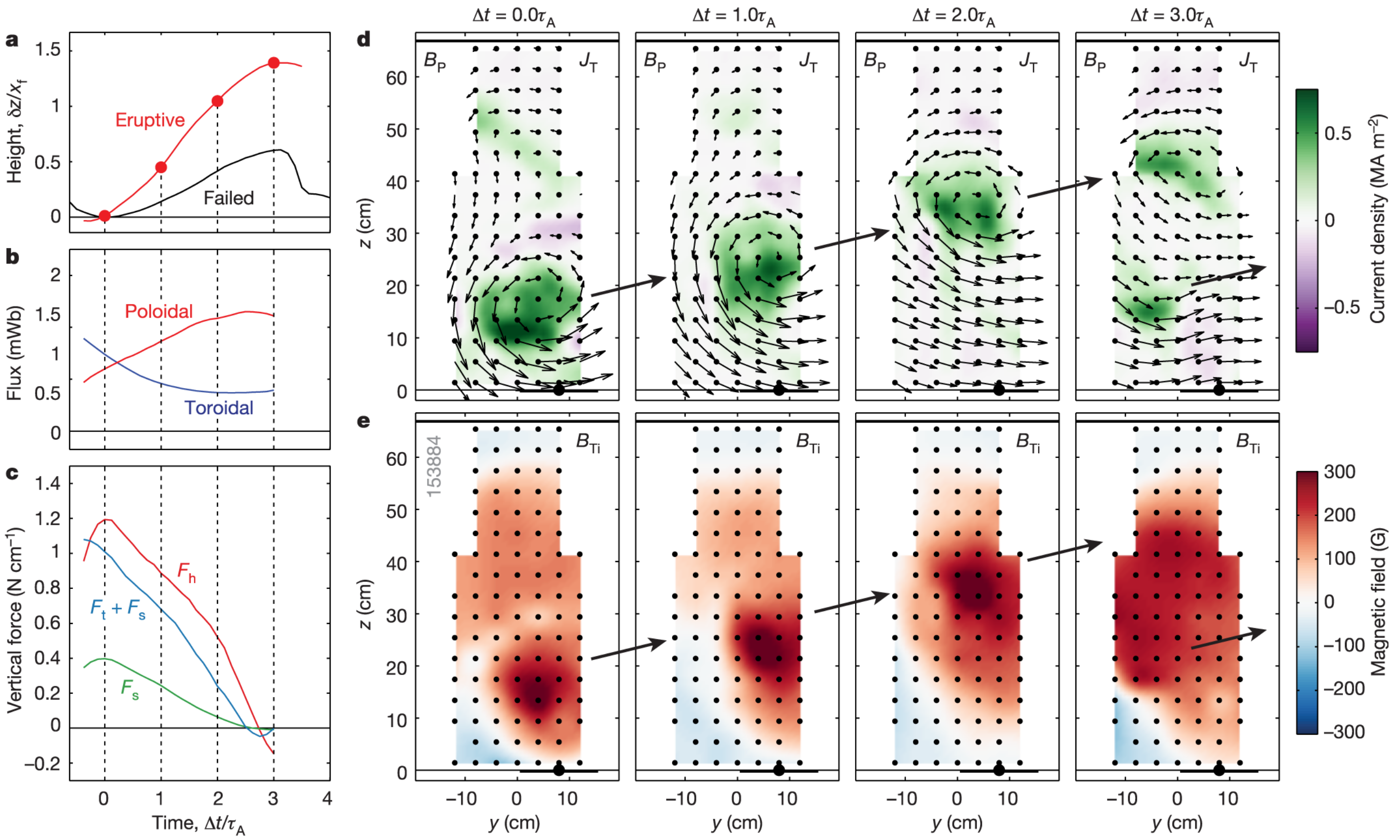

Extended Data Figure 3 | Magnetic field analysis of a characteristic eruptive event. **a**, The spatial evolution of the eruptive perturbation (red), with the failed torus event from Fig. 3a for comparison (black). **b**, Evolution of the poloidal and toroidal magnetic fluxes. Note the monotonic evolution of both fluxes. **c**, Hoop (F_h), strapping (F_s), and tension (F_t) force evolution, which are also strictly monotonic. **d**, **e**, Sequenced J_T and B_{Ti} evolution. Note that the current profile remains uniform and rises steadily towards the wall of the machine. A new flux rope is forming at low altitude in the final frame.

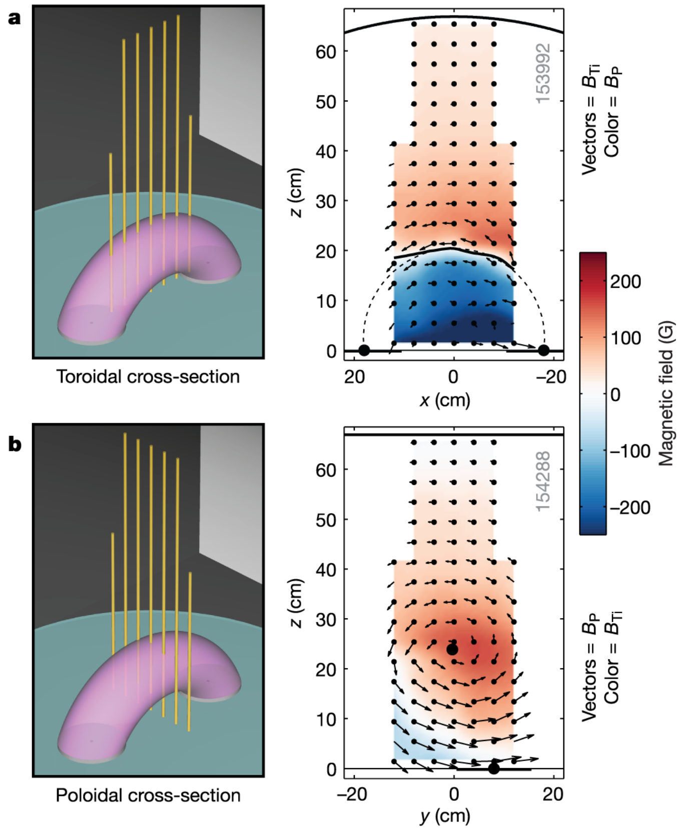

Extended Data Figure 4 | Sample *in situ* magnetic field measurements. Seven linear magnetic field probes (yellow) are inserted vertically into the flux rope plasma. The alignment of the two-dimensional probe plane is either (**a**) parallel to the footpoint axis or (**b**) perpendicular to it. In the sample data, the colour represents the out-of-plane field, while the vectors represent the in-plane field. The position of the magnetic axis In the toroidal cross-section (the solid black line) is determined by the reversal in the out-of-plane poloidal magnetic field, B_y. The position of the magnetic axis in the poloidal cross-section is defined as the O-point in the circulating in-plane field (B_y,B_z). The out-of-plane field in the latter case is the ‘internal’ toroidal field of the flux rope B_{Ti}, which is paramagnetic in nature.

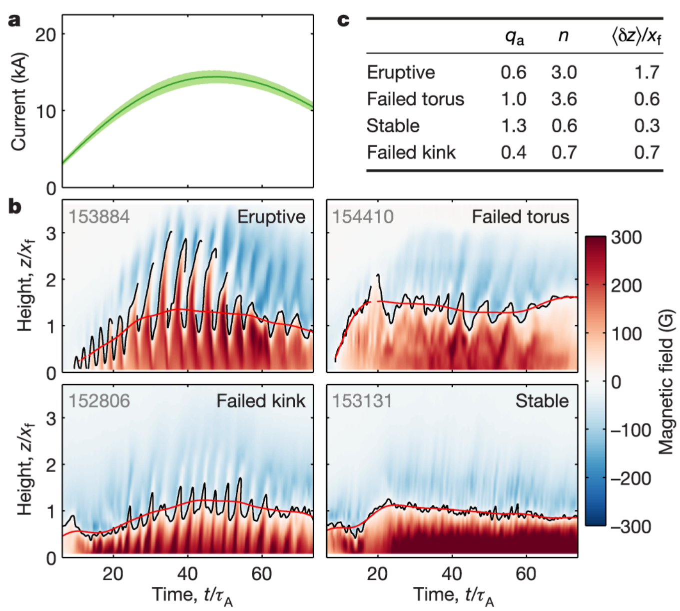

	q_a	n	$\langle \delta z \rangle / x_f$
Eruptive	0.6	3.0	1.7
Failed torus	1.0	3.6	0.6
Stable	1.3	0.6	0.3
Failed kink	0.4	0.7	0.7

Extended Data Figure 5 | Height-time plots from four representative flux rope discharges. a, Mean toroidal plasma current waveform showing that the plasma current is nearly the same in all four cases (the green band is the standard deviation). **b**, Four sample height-time plots, one from each of the four stability regimes identified in Fig 2. The magnetic axis position (the black line) is defined by the zero-crossing in the $B_y(t, z)$ data, which is shown in colour. The red line in each frame is the time-averaged height of the flux rope apex $\langle z_{apex} \rangle$. This waveform provides the height where q_a and n are measured in each discharge. **c**, Table of extracted flux rope parameters for each discharge.

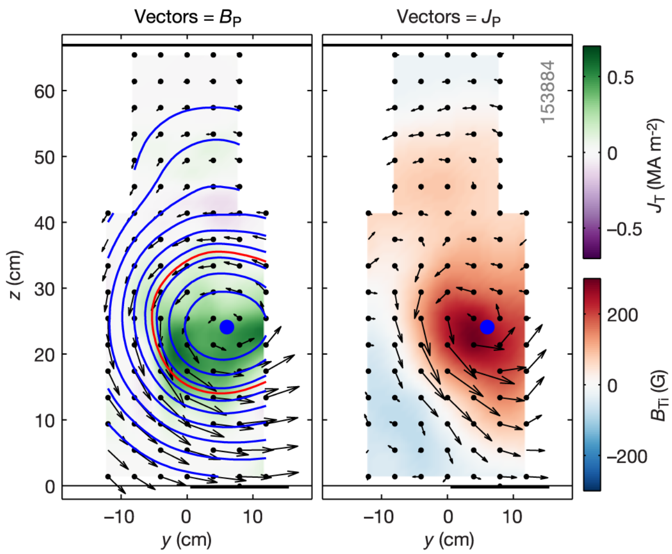

Extended Data Figure 6 | Magnetic field and current density data for computing flux rope forces. The probe array is aligned as shown in Extended Data Fig. 4b. In the left panel, the colour is the toroidal current density, J_T, and the vectors are the poloidal magnetic field, B_P. In the right panel, the colour is the internal toroidal field B_{Ti}, and the vectors are the poloidal current density J_P. With all components of $\mathbf{J}$ and $\mathbf{B}$ measured, the force densities listed in Extended Data Table 3 can be readily computed. The contours in the left panel are contours of the poloidal flux function $\psi(y, z)$ (see equation (4)). The minor radius of the rope $a(\theta)$ is defined by the poloidal flux contour shown in red (see Methods).

Laboratory parameter	Symbol	Value	Units
Magnetic field strength	B	300–500	G
Neutral density	n_n	~5×10^{14}	cm^{-3}
Electron density (approx.)	n_e	5×10^{13}–1×10^{14}	cm^{-3}
Electron temperature (approx.)	T_e	3–5	eV
Footpoint-to-footpoint scale length	L	0.5	m
Alfvén velocity	v_A	65–150	km/s
Alfvén transit time	τ_A	3–8	μs
Footpoint driving time	τ_D	~150	μs
Resistive diffusion time (Spitzer)	τ_R	0.8–2	ms

Extended Data Table 1 | Laboratory flux rope parameters. The quoted magnetic field strength, B, represents the footpoint-to-footpoint average along the rope. The electron density, n_e, and temperature, T_e, are approximate, owing to the limited availability of Langmuir probe data from these arc discharge plasmas. The characteristic footpoint driving time, τ_D, is set by the the capacitance, inductance, and resistance of the combined capacitor bank and plasma arc circuit. The laboratory parameters in this table are used to compute the related dimensionless parameters in Extended Data Table 2.

Dimensionless parameter	Symbol	Solar	Laboratory
Footpoint driving time / Alfvén transit time	τ_D/τ_A	100–10^4	20–50
Footpoint driving time / resistive diffusion time	τ_D/τ_R	10^{-7}	~0.1
Ion gyroradius / minor radius	ρ_i/a	10^{-6}	0.05
Electron mean free path / plasma length	λ_{ei}/L	10^{-2}	10^{-3}–10^{-2}
Lundquist number	S	10^4–10^{12}	100–500
Ionisation fraction	$n_e/(n_e+n_n)$	50–100%	10–20%
Plasma beta (thermal pressure / magnetic pressure)	β	~1%	2–20%

Extended Data Table 2 | Comparison of solar and laboratory dimensionless parameters. While the laboratory experiments are not able to replicate the extreme parameters of the corona, they do satisfy the key dimensionless limits required to produce storage-and-release eruptions that are driven by ideal magnetohydrodynamic instabilities (see Methods).

Quantity	Symbol	Expression
Strapping magnetic field (potential)	$\boldsymbol{B}_{\mathrm{s}}$	–
Internal poloidal magnetic field (flux rope)	$\boldsymbol{B}_{\mathrm{Pi}}$	–
Guide magnetic field (potential)	$\boldsymbol{B}_{\mathrm{g}}$	–
Internal toroidal magnetic field (flux rope)	$\boldsymbol{B}_{\mathrm{Ti}}$	–
Total poloidal magnetic field	$\boldsymbol{B}_{\mathrm{P}}$	$\boldsymbol{B}_{\mathrm{s}} + \boldsymbol{B}_{\mathrm{Pi}}$
Total toroidal magnetic field	$\boldsymbol{B}_{\mathrm{T}}$	$\boldsymbol{B}_{\mathrm{g}} + \boldsymbol{B}_{\mathrm{Ti}}$
Toroidal current density	$\boldsymbol{J}_{\mathrm{T}}$	$\nabla \times \boldsymbol{B}_{\mathrm{Pi}}/\mu_0$
Poloidal current density	$\boldsymbol{J}_{\mathrm{P}}$	$\nabla \times \boldsymbol{B}_{\mathrm{Ti}}/\mu_0$
Hoop force density (upward)	f_{h}	$\hat{\boldsymbol{e}}_z \cdot (\boldsymbol{J}_{\mathrm{T}} \times \boldsymbol{B}_{\mathrm{Pi}})$
Strapping force density (downward)	f_{s}	$\hat{\boldsymbol{e}}_z \cdot (\boldsymbol{J}_{\mathrm{T}} \times \boldsymbol{B}_{\mathrm{s}})$
Tension force density (downward)	f_{t}	$\hat{\boldsymbol{e}}_z \cdot (\boldsymbol{J}_{\mathrm{P}} \times \boldsymbol{B}_{\mathrm{T}})$

Extended Data Table 3 | Decomposition of magnetic field, current density, and force terms. This decomposition is chosen so that the quantities can be grouped into those related to the poloidal magnetic field ($\mathbf{B}_s$, $\mathbf{B}_{Pi}$, $\mathbf{J}_T$, f_h, and f_s) and those related to the toroidal magnetic field ($\mathbf{B}_g$, $\mathbf{B}_{Ti}$, $\mathbf{J}_P$, and f_t). The force densities, f, are integrated to force per-unit-length, F, before being compared (see Methods). Note that for simplicity, scalar representations of the vector components of $\mathbf{B}$ and $\mathbf{J}$ are used in the main text (for example, $B_T \equiv \hat{\mathbf{e}}_T \cdot \mathbf{B}_T$).

Supplemental Video 1 | Representative stable and erupting flux rope discharges. *Top left:* Experimental setup showing the pink arched flux rope attached to two conducting footpoints. The yellow vertical lines represent the *in situ* magnetic probes (see Methods). *Bottom left:* Height-time histories of the two flux rope discharges. *Right:* Frame sequences with the measured out-of-plane magnetic field overlaid on corresponding fast camera visible light images. The measured magnetic axis locations (the solid lines) are defined by the reversal of the out-of-plane magnetic field (see Methods). See Fig. 1 for a breakout of individual frames from this video.

Princeton Plasma Physics Laboratory
Office of Reports and Publications

Managed by
Princeton University

under contract with the
U.S. Department of Energy
(DE-AC02-09CH11466)

P.O. Box 451, Princeton, NJ 08543
Phone: 609-243-2245
Fax: 609-243-2751

E-mail: publications@pppl.gov

Website: http://www.pppl.gov